

# Coexistence of superconductivity with partially filled stripes in the Hubbard model

Hao Xu,<sup>1,\*</sup> Chia-Min Chung,<sup>2,3,4,\*</sup> Mingpu Qin,<sup>5</sup> Ulrich Schollwöck,<sup>6,7</sup> Steven R. White,<sup>8</sup> and Shiwei Zhang<sup>9</sup>

<sup>1</sup>*Department of Physics, College of William and Mary, Williamsburg, Virginia 23187, USA*

<sup>2</sup>*Department of Physics, National Sun Yat-sen University, Kaohsiung 80424, Taiwan*

<sup>3</sup>*Center for Theoretical and Computational Physics,*

*National Sun Yat-Sen University, Kaohsiung 80424, Taiwan*

<sup>4</sup>*Physics Division, National Center for Theoretical Sciences, Taipei 10617, Taiwan*

<sup>5</sup>*Key Laboratory of Artificial Structures and Quantum Control,*

*School of Physics and Astronomy, Shanghai Jiao Tong University, Shanghai 200240, China*

<sup>6</sup>*Arnold Sommerfeld Center for Theoretical Physics,*

*Ludwig-Maximilians-Universität München, 80333 Munich, Germany*

<sup>7</sup>*Munich Center for Quantum Science and Technology (MCQST), 80799 Munich, Germany*

<sup>8</sup>*Department of Physics and Astronomy, University of California, Irvine, California 92697, USA*

<sup>9</sup>*Center for Computational Quantum Physics, Flatiron Institute, New York, NY 10010, USA*

Combining the complementary capabilities of two of the most powerful modern computational methods, we find superconductivity in both the electron- and hole-doped regimes of the two-dimensional Hubbard model (with next nearest neighbor hopping). In the electron-doped regime, superconductivity is weaker and is accompanied by antiferromagnetic Néel correlations at low doping. The strong superconductivity on the hole-doped side coexists with stripe order, which persists into the overdoped region with weaker hole density modulation. These stripe orders, neither filled as in the pure Hubbard model (no next nearest neighbor hopping) nor half-filled as seen in previous state-of-the-art calculations, vary in fillings between 0.6 and 0.8. The resolution of the tiny energy scales separating competing orders requires exceedingly high accuracy combined with averaging and extrapolating with a wide range of system sizes and boundary conditions. These results validate the applicability of this iconic model for describing cuprate high- $T_c$  superconductivity.

## I. INTRODUCTION

Does the Hubbard model qualitatively capture the essential physics of the high temperature superconducting cuprates? This question has been debated since shortly after these materials were discovered [1–10]. As the decades have passed it has become clearer that the answer has to come from simulations powerful enough to give definitive results on the properties of the model, so that one can see whether these properties match those observed experimentally. This has proved to be especially difficult because the ground states of the models have been shown to be exceptionally sensitive to small changes in the model terms and parameters, with competing [11] or cooperating [12] charge, spin [13], and superconducting (SC) orders [14–18]. The relevant model parameters are in the most difficult regime – moderately strongly-coupled – where most approaches struggle. The frequent presence of stripes in the ground states increases the sizes of the clusters needed to extrapolate to the thermodynamic limit.

A powerful tool has emerged to help overcome these difficulties: the use of combinations of simulation methods with complementary strengths and weaknesses [19]. The density matrix renormalization group (DMRG) [20–22] provides the most accurate and reliable results when applied on fairly narrow cylinders [23]. Other methods

work either directly in the thermodynamic limit [24, 25] or at least on much wider clusters [26], but have approximations tied to unit cell size [24, 27, 28], coupling strength, etc [25, 29, 30]. The constrained path (CP) auxiliary field quantum Monte Carlo (AFQMC) method [26, 31, 32] is particularly complementary to DMRG: it can be used on much wider systems; the errors from CP to control the sign problem have been consistently modest [19]; and the underlying approximation of CP is unrelated to the low entanglement approximation of DMRG. AFQMC is based on a wave picture of superposition of Slater determinants, while DMRG is rooted in the particle picture with strong coupling. Their quantitative handshake proved to be crucial for uncovering the delicate nature of the stripe correlations as we discuss below. Previously, we used this combination, extrapolating to the two-dimensional thermodynamic limit, to find that superconductivity is absent in the pure (i.e., with no next nearest-neighbor hopping) Hubbard model [11]. In that case, the lack of superconductivity was tied to the occurrence of filled striped states [33].

Here, we apply this approach, with new developments, to tackle the Hubbard model with a non-zero next nearest-neighbor hopping,  $t'$ . In connection to the typical phase diagram of cuprates, a nonzero  $t'$  is necessary to account for the particle-hole asymmetry and the band structures. The  $t' \neq 0$  model is significantly more difficult computationally, with challenges for both DMRG and AFQMC. Where both methods apply, DMRG certifies the high accuracy and reliability of AFQMC as used here. As discussed below, in cases of ambiguity (e.g., in some width-6 cylinders), resolving the discrepancies

---

\*These two authors contributed equally to this work.

has often created new synergy between the two methods, and led to new insights. The phase diagram with  $t'$  also turns out to be significantly more complicated, with partially filled stripes coexisting with superconductivity on the hole-doped side, and uniform antiferromagnetic order coexisting with superconductivity on the electron side. The final results for superconductivity, extrapolated to the thermodynamic limit, are impressively similar to the properties of cuprates, with both electron and hole doped SC “domes”, but with the hole doped side being significantly stronger.

The Hamiltonian of the Hubbard model is

$$\hat{H} = -t \sum_{\langle ij \rangle, \sigma} \hat{c}_{i\sigma}^\dagger \hat{c}_{j\sigma} - t' \sum_{\langle\langle ij \rangle\rangle, \sigma} \hat{c}_{i\sigma}^\dagger \hat{c}_{j\sigma} + U \sum_i \hat{n}_{i\uparrow} \hat{n}_{i\downarrow} - \mu \sum_{i\sigma} \hat{n}_{i\sigma} \quad (1)$$

where  $i$  or  $j$  labels a site on a square lattice,  $\hat{c}_{i\sigma}^\dagger$  is the electron creation operator,  $\sigma = \{\uparrow, \downarrow\}$  denotes spin,  $\hat{n}_{i\sigma} = \hat{c}_{i\sigma}^\dagger \hat{c}_{i\sigma}$  is the particle-number operator, and  $\langle ij \rangle$  and  $\langle\langle ij \rangle\rangle$  indicate nearest- and next-nearest-neighbors, respectively. We set  $t$  as the energy unit. In cuprates  $t' < 0$  [34]; however, using a particle-hole transformation to map fillings  $1+\delta \rightarrow 1-\delta$ , we can study electron doping by changing the sign of  $t'$ . We use  $t' = -0.2$  for hole-doping and  $t' = +0.2$  for electron-doping, appropriate values for cuprates based on band structure calculations [35, 36]. The onsite repulsion  $U$  is fixed at  $U = 8$ , again a representative value for cuprates. We scan a range of doping (denoted by  $\delta$ ) by varying  $\mu$ .

Our study focuses on the ground state, which we obtain in either cylindrical or fully periodic systems. The use of cylinders serves two purposes. First they allow direct comparisons between AFQMC and DMRG, which is highly accurate in narrow cylinders. Second, they are convenient for studying spin and charge orders, in which we apply spin-symmetry-breaking pinning fields on the edges of the cylinder to help detect ordering from the resulting local spin and charge densities. The fully periodic simulation cells allow AFQMC to better approach the thermodynamic limit (TDL). As shown below, it turns out to be crucial to systematically average over different boundary conditions. To compute the pairing order parameter, we apply twist averaged boundary conditions (TABC) over a large number of random twists, in systems with up to 500 lattice sites. The computations presented in this work became possible only with new algorithmic developments in both our methods, which improved capability and increased accuracy, as we discuss further in the Method Section.

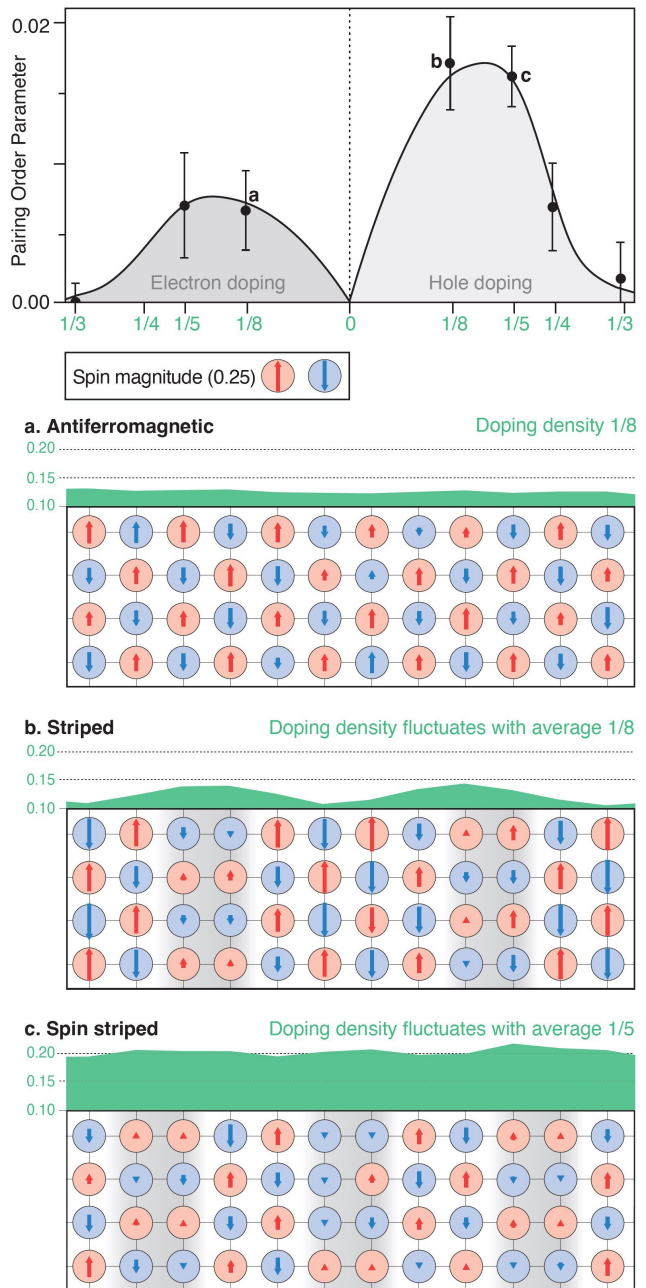


FIG. 1: The  $d$ -wave pairing order parameter versus doping  $\delta$  in the ground state for the hole-doped ( $t' = -0.2$ ) and electron-doped ( $t' = +0.2$ ) regimes. Representative spin and charge correlations are also shown for three parameter sets a, b, and c.  $\Delta_d$  are the spontaneous pairing order in the thermodynamic limit, while the spin and charge (hole) patterns are drawn from the middle of  $28 \times 8$  (a),  $24 \times 8$  (b), and  $40 \times 8$  (c) cylinders with antiferromagnetic spin pinning fields applied to the two edges. Note that hole densities start at 0.1. Grey shadows for spins are to aid the eye.

## II. RESULTS

### A. Overview of pairing and coexisting spin/charge orders

Figure 1 presents an overview of our results, a “phase diagram” of the computed pairing order parameter, together with representative spin and charge correlations. The pairing order parameters have been extrapolated to the TDL, using full TABC in large simulation cells (see Method and SM). We expect this zero-temperature property to be loosely connected to the transition temperature  $T_c$  most readily observed experimentally (however, see [37, 38]). On both the electron- and hole-doped sides, we find dome-like  $d$ -wave pairing orders which resemble the  $T_c$  domes in the typical phase diagram of cuprates. The pairing order is significantly larger in the hole-doped region than in the electron-doped region, which is also consistent with the phase diagram of cuprates [39]. Spin and hole densities are shown for the three representative systems marked as a, b, and c. These calculations were performed with AFM pinning fields on the edges of the cylindrical simulation cells (details in SM). The spin and hole densities thus provide a simple and convenient way to visualize the spin and charge correlations. We have taken care to ensure that the results are drawn from very large systems and the spin and charge patterns are representative of different boundary conditions. In the electron-doped region, the spins show single-domain antiferromagnetism with nearly uniform hole densities in the bulk. In the hole-doped region, stripe and spin-density wave (SDW) correlations are observed, with modulated antiferromagnetic domains separated by phase flip lines where holes are more concentrated. In contrast with the pure Hubbard model, we find that the wavelength of the modulation is not an integer multiple of  $1/\delta$  (filled stripes). Nor are the stripes half-filled as seen in previous state-of-the-art calculations [40]. Rather, they are best described as partially filled, with fractional fillings which vary with  $\delta$  as well as system size and boundary conditions. These behaviors of spin and charge are again consistent with the phase diagram of the cuprates [39], where uniform AF correlations persist with substantial doping on the electron-doped side, but short or long-ranged incommensurate magnetism and stripes are observed starting at small doping on the hole-doped side [41, 42].

This phase diagram contrasts sharply with that of the  $t$ - $t'$ - $J$  model[43, 44], which can be derived as an approximate strong-coupling Hubbard model at low doping. In the  $t$ - $t'$ - $J$  model, recent DMRG studies all point to strong  $d$ -wave superconductivity on the electron-doped side [43–45], which coexists with antiferromagnetic correlations with increasing strength as  $t'$  increases; some differences remain concerning whether long-range AF order occurs [46]. No superconductivity, only stripes, have been found on the hole-doped side. It has been an open question whether this failure of the  $t$ - $t'$ - $J$  model to qualitatively

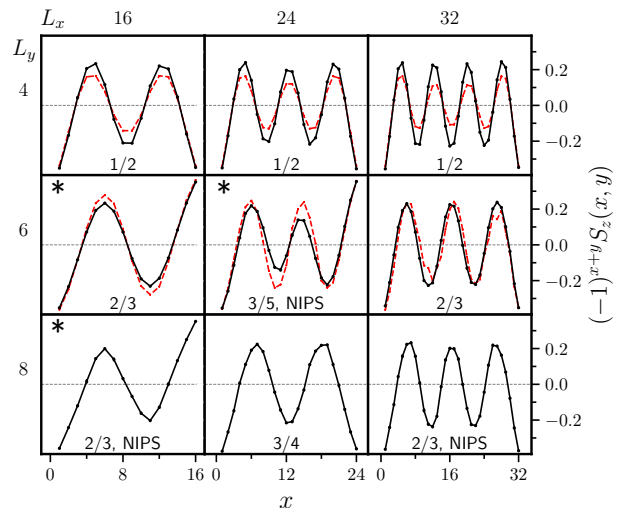


FIG. 2: Evolution of the stripe patterns with system size ( $\delta = 1/8$ , hole-doped). The staggered spin densities are shown as linecuts in periodic cylinders. The length of the cylinder ( $L_x$ ) is varied across the three columns and the width ( $L_y$ ) across rows. AFM pinning fields are applied at the two edges of the cylinder ( $x = 1$  and  $x = L_x$ ), either in phase or with a  $\pi$ -phase shift (marked by an asterisk); the one with lower energy is shown. The filling fraction  $f$  of each stripe pattern is indicated, with NIPS denoting non integer-pair stripes. DMRG results (red) are shown for width-4 and 6 systems and AFQMC results (black) are in good agreement with them.

explain the cuprates was due to the strong-coupling approximations of that model, or to other flaws or missing terms affecting both the Hubbard and  $t$ - $t'$ - $J$  (single band) models. Here the strong differences in the phase diagrams of the two models point to the former. These differences have not been clear in previous studies on narrower cylinders, which are impacted by strong finite-size effects [47, 48].

### B. Underdoped region: 1/8 hole doping

A relatively large pairing order parameter is found here, in coexistence with stripe correlations, as shown in Fig. 1. To better understand the nature of the spin and charge correlations, we systematically study their evolution with system sizes in Fig. 2. The computations were performed in  $L_x \times L_y$  cells, with periodic (PBC) or anti-periodic boundary condition (APBC) in the  $\hat{y}$ -direction and open BC along  $\hat{x}$  (i.e., cylinders). AFM pinning fields (along  $\hat{z}$ ) were applied at  $x = 1$  and  $L_x$  to break the  $SU(2)$  symmetry and induce local spin orders, such that the local spin density  $S_z(x, y)$  becomes a proxy of spin-spin correlations away from the edges of the cylinder.

Modulated AFM patterns are clearly seen in all the systems. Correspondingly, hole densities are enhanced at the nodes of the spin modulation, as illustrated in Fig. 1

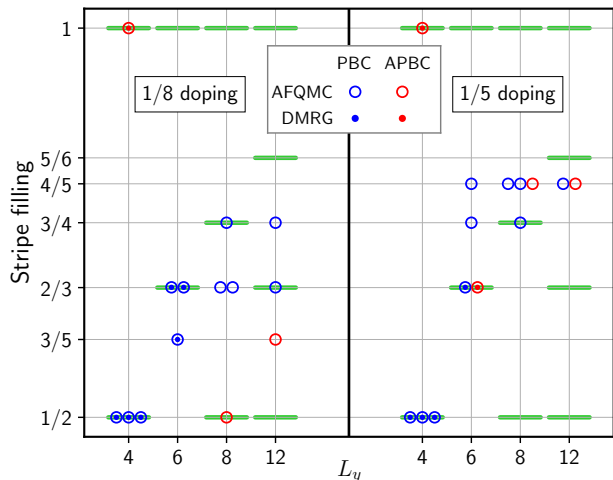


FIG. 3: Partially filled stripe patterns on the hole-doped side, at  $\delta = 1/8$  and  $1/5$ . The stripe fillings are shown for a variety of system sizes, in cylindrical cells with width  $L_y = 4$  up to 12, and lengths ranging from 16 to 48 (shown as adjacent symbols at fixed  $L_y$ ). Results for both PBC and APBC are shown. Narrow cylinders favor integer-pair stripes (IPS, indicated by green bars). Fluctuations are strong even in large systems.

(results on the corresponding hole densities for Fig. 2 can be found in SM). The characteristic wavelength of the modulation,  $\lambda_{\text{SDW}}$ , varies with system size. We define a filling fraction of the stripe:  $f \equiv \delta \lambda_{\text{SDW}}/2$ , i.e., the number of holes per lattice spacing along a stripe. In the pure Hubbard model,  $f = 1$  since  $\lambda_{\text{SDW}} = 2/\delta$  [49, 50]. Then, *nominally* the number of electron pairs per stripe is  $n_p \equiv f L_y/2$ . If  $n_p$  is an integer, we refer to the state as integer-pair stripe (IPS); otherwise the state is labeled as non-IPS (NIPS).

Previous studies in width-4 cylinders have found that the ground state in this system has half-filled stripes [40, 43, 44]. Our results confirm this picture, with good agreement between AFQMC and DMRG, but also show that the half-filled stripe turns out to be special to width-4. As the system size increases, the stripe filling fluctuates between  $3/5$  and  $3/4$ . NIPS states appear frequently, which have not been observed before. Previous calculations [11, 51] show that states with IPS are favored, which was taken as an indication of the existence of local pairing of electrons in the stripe state. Here, with the inclusion of  $t'$ , the electron is more mobile and pairs of electrons become coherent to display long-range pairing order. This is further discussed and contrasted with the over-doped region next.

### C. Overdoped region: $1/5$ hole doping

A strong superconducting order parameter is found in the ground state of the hole overdoped region of  $\delta = 1/5$ , with strength comparable to  $\delta = 1/8$  (see Fig. 1). The

behavior of spin and charge correlations show common features but also significant differences between the two regions. Figure 3 summarizes their stripe fillings side by side, based on computations in about 30 systems. Several trends are evident. In narrow cylinders, IPS states are favored at both dopings. In over a dozen different width-4 and width-6 systems across the two dopings, AFQMC and DMRG agree in each case on the stripe wavelength and filling fraction. In both regimes the filling fraction varies widely with system sizes and boundary conditions, and fluctuations continue through systems with over 500 lattice sites. As the size grows (wider cylinders), IPS states are no longer favored, and both systems tend to fractional stripe fillings. These results indicate that with  $t'$ , the stripe patterns — but not the existence of stripes — are much more fragile than in the pure Hubbard model.

Both the spin and charge modulations are weaker at  $1/5$  doping than at  $1/8$ . Although  $f$  is larger in the TDL, the holes are more mobile and spread out in the overdoped region. The hole density is nearly uniform, with less than 5% of the holes contributing to the density fluctuations. At  $1/8$  doping, the stripe order is more pronounced, as illustrated in Fig. 1. Still, the peak density of holes, at the nodes of the spin correlation, is only  $\sim 30\%$  higher than the average. The notion of stripe filling derives from a particle picture, most applicable to holes in Wigner-crystal-like distributions. The holes here have a strong wave character [49], with which the fractional fillings of stripes we observe are more readily compatible.

### D. Electron doped region

Experimentally, the electron-doped side is simpler, without the competing stripe state [41, 52] or pseudogap phase in cuprates [39]. The critical doping for the long-range AF order on the electron-doped side is larger than that on the hole-doped side, the superconducting dome is smaller, and the transition temperature is lower. The phase diagram in Fig. 1 and the spin and hole densities in Fig. 4 are consistent with these features.

Our results reveal several other important features on the electron-doped side. There are considerable variations of the spin and charge correlations with system sizes and boundary conditions, even though the sensitivity is less compared to the hole-doped side. As illustrated in the SM, two entirely different ground-state orders are obtained from width-4 and width-6 cylinders; APBC and PBC also lead to opposite conclusions in each simulation cell. Even in the width-8 systems in Fig. 4, which display robust Néel order, different boundary conditions still show variations in the charge correlation. Superconductivity manifests a more dramatic volatility. Using PBC, the most common approach to date, calculations in width-4 and width-6 cylinders would conclude a strong pairing order in the electron-doped regime. (Note that



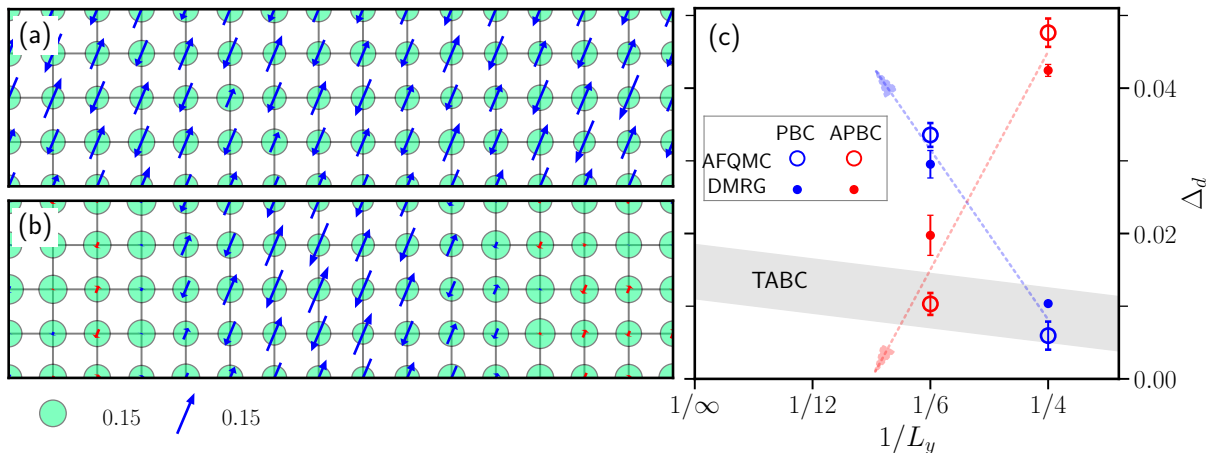


FIG. 4: Spin, charge, and pairing properties on the electron doped side ( $\delta = 1/8$ ), and their variations with boundary conditions. (a) APBC along  $\hat{y}$ -direction in a  $28 \times 8$  cylinder gives nearly uniform Neel order (only a  $16 \times 4$  central region is shown). (b) Under PBC a modulated AFM order with larger spatial variations in spin magnitude is seen. (c) The computed pairing orders in  $16 \times 4$  and  $16 \times 6$  cylinders (at a fixed value  $h_d = 0.021$  of applied global  $d$ -wave pairing fields) show opposite trends with PBC and APBC. The final pairing order, computed from TABC with fully periodic supercells of increasing  $L_y$ , is shown together with the TDL extrapolation by the gray band.

DMRG and AFQMC give fully consistent results.) In contrast, under APBC the same calculations predict no pairing. The uncertainties with respect to finite size and boundary conditions are much larger than the final signal at the TDL. Thus even a qualitative conclusion on superconductivity would be challenging without our new approaches employing TABC, systematic extrapolation to large sizes, and other methodological advances, which are discussed next.

### III. METHOD

The physics of the Hubbard model has proved highly elusive and challenging to pin down. This was magnified substantially with a non-zero  $t'$ . The difficulties include more sensitivity and stronger dependency on system size and BC, as we have illustrated. In addition,  $t'$  turns out to affect the interplay between low-lying states in significant ways. For instance, with  $t' = 0$ , stripe and superconductivity manifest as competing orders. Filled stripe states are particularly stable, with nesting contributing a key factor. A non-zero  $t'$  affects the nesting condition (frustrates the Néel order) and alters the landscape of the low-lying states. This has demanded much higher resolution from the numerical methods.

The methodologies employed in this work have a number of distinguishing features which made it possible to achieve a qualitatively higher level of accuracy and reliability. Two complementary, state-of-the-art computational methods are used synergistically. We implement both U(1) [53] and SU(2) symmetry-adapted [54] DMRG calculations for different setups and push them to the large bond-dimension limit. In AFQMC, we introduce

a further advance in the optimization of the constraining trial wave function, which is determined fully self-consistently [32], with no input parameter. Extensive and detailed comparisons between AFQMC and DMRG are performed on width-4 and width-6 cylinders, under identical conditions. The same AFQMC algorithm, which has no room for tuning, is applied to larger systems. The formulation of systematic twist averaging for the computation of the pairing order parameters provides an effective way to sample the low-lying states.

#### A. Twist averaging as an effective means to sample low-lying states

The use of twist-averaging [55, 56] in this work has two crucial roles. First, systematically averaging over twist angles, combined with the ability to reach large system sizes and careful finite size extrapolation, enables us to approach the TDL reliably. Second, the random twist angles provide an effective means to sample the low-lying states, and their averaging reduces the impact of rare events of accidental degeneracy, and smoothes out the effect of level crossings as a function of an applied pairing field (see SM).

As shown in Fig. 4, different boundary conditions can result in variations in the pairing order parameter which are many times larger than the signal, even in nominally rather large sizes (width-6 cylinders). Both PBC and APBC are twist angles of special symmetry, and are often particularly volatile. We apply TABC with quasi-random twist angles [56]. The TBC can be thought of as the electron gaining a phase when it crosses the boundary. Equivalently, we can choose another gauge by dis-

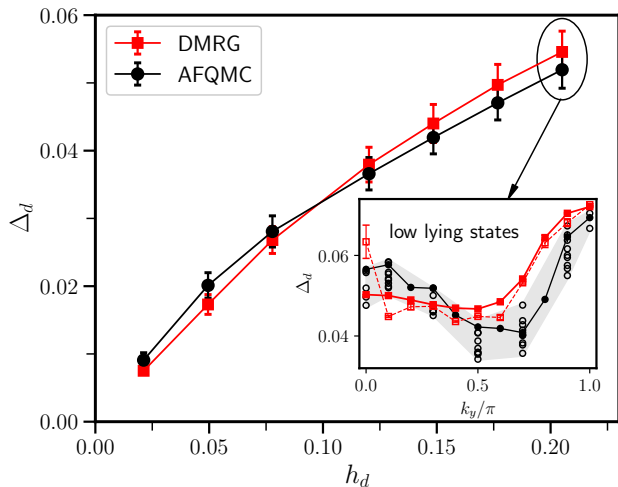


FIG. 5: Importance of TABC for accurate determination of the pairing order. The main figure shows the  $d$ -wave pairing order parameters in a  $20 \times 4$  cylindrical cell at  $1/5$  hole doping, after full twist-averaging over  $k_y$ . AFQMC and DMRG results agree across the entire range of  $h_d$ , the strength of the applied pairing fields. The inset focuses on  $h_d = 0.205$ .  $\Delta_d$  computed from DMRG and AFQMC are shown as a function of  $k_y$ , for the ground state (connected by solid line) and some of the lowest-lying excited states (open symbols). Averages of the solid symbols lead to the TABC results in the main figure.

tributing the phase evenly in each hopping term. When a twist is applied, care must be taken in defining the pairing order parameter, whose form is gauge-dependent but the expectation value should be gauge-independent. TABC reduces the fluctuations in the computed pairing order parameter, as seen in Fig. 4, and further discussed below and in the SM. (In Ref. [57], TBC and twist averaging are shown to accelerate the extrapolation with calculations on cylinders.)

With the inclusion of a non-zero  $t'$ , the perfect nesting in the Fermi surface at half-filling is absent. Subtle variations near the Fermi level from finite size and boundary conditions can have much larger effect on the formation of collective spin modes, hence there is more sensitivity in the property of the low-lying states. These states can be very close in energy such that any small finite temperature (e.g., under experimental conditions) would smear them out and render them indistinguishable. TABC provides an effective sampling of such low-lying states which can average out the fluctuations so as to more reliably capture the intrinsic properties. An illustration is given in Fig. 5. The pairing order parameter exhibits large variations as a function of the twist angle, both in the ground state and low-lying excited states, as seen in the inset for one value of  $h_d$ . The calculation can “hop” from one state to another among the bundle of low-lying states, depending on the initial condition, convergence criterion, etc, even under high-quality computational settings (e.g., large bond dimensions in DMRG).

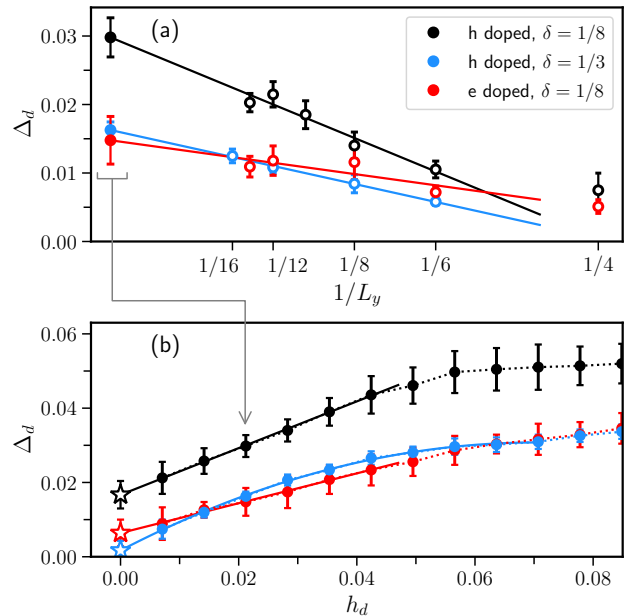


FIG. 6: Computation of the ground-state pairing order parameter at the thermodynamic limit. (a) shows extrapolation to the TDL at a fixed  $h_d$ , the strength of the  $d$ -wave pairing fields. (b) shows extrapolation of the TDL result from (a) to  $h_d \rightarrow 0$ . Three representative systems are shown. In (a), each data point is obtained by TABC over  $(k_x, k_y)$  in supercells of  $L_x \times L_y$ , and only results from large supercells are included. In (b) linear or quadratic fits are performed at small values of  $h_d$ , with extrapolated values marked as stars.

This is also reflected in the modest level of agreement between the two methods for each particular state. With TABC, however, their agreement is excellent across the entire range of  $h_d$  (which spans many level-crossings, see SM), and the two methods give fully consistent conclusions.

## B. Extrapolation of pairing order

The spontaneous pairing order parameter in the TDL,  $\Delta_d$ , is obtained from a massive number of computations. At each parameter set ( $t'$  and doping),  $\Delta_d(N, h_d)$  is computed for many different simulation cell sizes  $N$ , at tens of  $h_d$  values, with each averaged over tens of quasi-random twist angles. We then take the limit  $\Delta_d(N \rightarrow \infty, h_d)$  at each  $h_d$ , followed by the extrapolation  $\Delta_d(\infty, h_d \rightarrow 0)$ . The procedure is illustrated in Fig. 6. Panel (a) shows the first step, where we use fully periodic  $N = L_x \times L_y$  systems with quasi-random twist angles  $(k_x, k_y)$  applied to both directions. We verify that  $L_x$  is sufficiently large such that the results have converged within our statistical accuracy. We then extrapolate the TABC results with respect to  $1/L_y$ , excluding small sizes. (Deviations are visible from width-4 systems, which can have different pairing symmetry from ordinary  $d$ -wave [48].) In Panel (b)

extrapolations are then performed using small  $h_d$  values ( $< 0.05$  for linear and last 10 or so points for quadratic fits), yielding the final spontaneous pairing order parameter  $\Delta_d$  at  $h_d \rightarrow 0$ . As can be seen, the quality of the fits is excellent; in each case, the linear and quadratic fits give consistent values within statistical errors.

#### IV. CONCLUSION

Can the single band Hubbard model capture the qualitative physics, particularly the superconductivity, of the cuprates? Here, more than 35 years after the discovery of the first cuprate superconductor [1], we conclude that the answer is yes, that the Hubbard model with a next near-neighbor hopping  $t'$  distinguishing between electron- and hole-doping captures the essential features of the charge, magnetic, and pairing orders.

The computed pairing order parameter in the ground state displays dome-like structures versus doping, resembling the  $T_c$  domes of the cuprates. On the hole-doped side, we find the coexistence of superconductivity with fractionally filled stripe correlations, with nominal stripe fillings in the range 0.6-0.8 in sufficiently large sizes. On the electron-doped side, at lower dopings, uniform or weakly modulated antiferromagnetism, along with uniform or weakly modulated doping, coexists with somewhat weaker superconductivity. The general appearance of stripe orders on the larger systems with non-integral numbers of pairs indicates that pairs fluctuate between stripes, promoting long-distance phase coherence and thus superconductivity; in contrast, for  $t' = 0$  the stripes were filled, and superconductivity was absent [11].

This picture is in contrast to that of the  $t$ - $t'$ - $J$  model, once thought to be interchangeable with the Hubbard model, but which does not appear to exhibit superconductivity on the hole-doped side [43–45]. The ground states of the models are not universal, and to capture the subtle interaction of the various intertwined orders requires both very careful finite size extrapolation and very high accuracy and reliability in the simulation methods. Even within the single-band  $t$ - $t'$  Hubbard model, an enormous body of works exists, with widely varying and often conflicting results. Our results also explain why this has been the case — the model shows extreme sensitivity of the properties to finite sizes and boundary conditions, and to any biases of approximate methods.

Here we have used the combination of DMRG and AFQMC, with DMRG benchmarking and validating the CP approximation in AFQMC on narrower systems and the AFQMC used to reach much larger systems. We have greatly improved the finite size extrapolations by using TABC. These together with methodological advances

within each approach provided a powerful tool to address the question with a new level of capability and resolution.

In the models or parameter regimes on the hole-doped side where superconductivity is not present, one still finds strong indications of paired holes. For example, if holes within stripes were not paired, one would expect to find single stripes having an odd number of holes in about half the systems, but instead only even numbers of holes in each stripe are found. Whether there is superconductivity or not seems tied to the properties of a pair, e.g., its effective mass, which is strongly influenced by model parameters such as  $t'$ . A heavy pair or one which interacts strongly with the magnetic degrees of freedom of the region around it is more likely to be locked up in a stripe, suppressing phase coherence. This model-specificity and non-universality raises the question: is there any simple analytic theory of cuprate superconductivity in the style of BCS, or must we always resort to simulation?

Our study still leaves much to do in connecting the models quantitatively to experiments. We have not predicted transition temperatures, only order parameters. We have not studied transport and dynamical properties of the models. Many other properties of the one-band Hubbard model remain to be determined and understood. Other terms [58, 59] and effects not present in the Hubbard model may still play important quantitative roles. Nevertheless, it appears that qualitatively, the  $t$ - $t'$ - $U$  Hubbard model has “the right stuff”.

#### V. ACKNOWLEDGMENTS

We thank A. Georges, S. Kivelson, A. J. Millis, M. Morales, H. Shi, E. Vitali, and T. Xiang for discussions. We are grateful to Lucy Reading-Ikkanda for help with graphics. M.Q. acknowledges the support from the National Key Research and Development Program of MOST of China (2022YFA1405400), the National Natural Science Foundation of China (Grant No. 12274290) and the sponsorship from Yangyang Development Fund. SRW acknowledges the support of the NSF through under DMR-2110041. US acknowledges funding by the Deutsche Forschungsgemeinschaft (DFG, German Research Foundation) under Germany’s Excellence Strategy-EXC-2111-390814868. H.X. thanks the Center for Computational Quantum Physics, Flatiron Institute for support and hospitality. The Flatiron Institute is a division of the Simons Foundation. C.-M.C. acknowledges the support by the Ministry of Science and Technology (MOST) under Grant No. 111-2112-M-110-006-MY3, and by the Yushan Young Scholar Program under the Ministry of Education (MOE) in Taiwan.

---

[1] J. G. Bednorz and K. A. Müller, *Zeitschrift für Physik B Condensed Matter* **64**, 189 (1986), ISSN 1431-584X,

URL <https://doi.org/10.1007/BF01303701>.

- [2] J. Hubbard, Proceedings of the Royal Society of London. Series A. Mathematical and Physical Sciences **276**, 238 (1963), URL <https://royalsocietypublishing.org/doi/abs/10.1098/rspa.1963.0204>.
- [3] P. W. Anderson, Science **235**, 1196 (1987), URL <https://www.science.org/doi/abs/10.1126/science.235.4793.1196>.
- [4] V. J. Emery, Phys. Rev. Lett. **58**, 2794 (1987), URL <https://link.aps.org/doi/10.1103/PhysRevLett.58.2794>.
- [5] F. C. Zhang and T. M. Rice, Phys. Rev. B **37**, 3759 (1988), URL <https://link.aps.org/doi/10.1103/PhysRevB.37.3759>.
- [6] P. W. Anderson and R. Schrieffer, Physics Today **44**, 54 (1991), <https://doi.org/10.1063/1.881261>, URL <https://doi.org/10.1063/1.881261>.
- [7] E. Dagotto, Rev. Mod. Phys. **66**, 763 (1994), URL <https://link.aps.org/doi/10.1103/RevModPhys.66.763>.
- [8] B. Keimer, S. A. Kivelson, M. R. Norman, S. Uchida, and J. Zaanen, Nature **518**, 179 (2015).
- [9] M. Qin, T. Schäfer, S. Andergassen, P. Corboz, and E. Gull, Annual Review of Condensed Matter Physics **13**, 275 (2022), <https://doi.org/10.1146/annurev-conmatphys-090921-033948>, URL <https://doi.org/10.1146/annurev-conmatphys-090921-033948>.
- [10] D. P. Arovas, E. Berg, S. A. Kivelson, and S. Raghu, Annual Review of Condensed Matter Physics **13**, 239 (2022), <https://doi.org/10.1146/annurev-conmatphys-031620-102024>, URL <https://doi.org/10.1146/annurev-conmatphys-031620-102024>.
- [11] M. Qin, C.-M. Chung, H. Shi, E. Vitali, C. Hubig, U. Schollwöck, S. R. White, and S. Zhang (Simons Collaboration on the Many-Electron Problem), Phys. Rev. X **10**, 031016 (2020), URL <https://link.aps.org/doi/10.1103/PhysRevX.10.031016>.
- [12] H.-C. Jiang and S. A. Kivelson, Proceedings of the National Academy of Sciences **119**, e2109406119 (2022), <https://www.pnas.org/doi/pdf/10.1073/pnas.2109406119>, URL <https://www.pnas.org/doi/abs/10.1073/pnas.2109406119>.
- [13] S. R. White and D. J. Scalapino, Phys. Rev. Lett. **91**, 136403 (2003), URL <https://link.aps.org/doi/10.1103/PhysRevLett.91.136403>.
- [14] E. Gull, O. Parcollet, and A. J. Millis, Phys. Rev. Lett. **110**, 216405 (2013), URL <https://link.aps.org/doi/10.1103/PhysRevLett.110.216405>.
- [15] A. S. Darmawan, Y. Nomura, Y. Yamaji, and M. Imada, Phys. Rev. B **98**, 205132 (2018), URL <https://link.aps.org/doi/10.1103/PhysRevB.98.205132>.
- [16] A. Himeda, T. Kato, and M. Ogata, Phys. Rev. Lett. **88**, 117001 (2002), URL <https://link.aps.org/doi/10.1103/PhysRevLett.88.117001>.
- [17] B. Ponsioen, S. S. Chung, and P. Corboz, Phys. Rev. B **100**, 195141 (2019), URL <https://link.aps.org/doi/10.1103/PhysRevB.100.195141>.
- [18] P. Corboz, T. M. Rice, and M. Troyer, Phys. Rev. Lett. **113**, 046402 (2014), URL <https://link.aps.org/doi/10.1103/PhysRevLett.113.046402>.
- [19] J. P. F. LeBlanc, A. E. Antipov, F. Becca, I. W. Bulik, G. K.-L. Chan, C.-M. Chung, Y. Deng, M. Ferrero, T. M. Henderson, C. A. Jiménez-Hoyos, et al. (Simons Collaboration on the Many-Electron Problem), Phys. Rev. X **5**, 041041 (2015), URL <https://link.aps.org/doi/10.1103/PhysRevX.5.041041>.
- [20] S. R. White, Phys. Rev. Lett. **69**, 2863 (1992), URL <https://link.aps.org/doi/10.1103/PhysRevLett.69.2863>.
- [21] S. R. White, Phys. Rev. B **48**, 10345 (1993), URL <https://link.aps.org/doi/10.1103/PhysRevB.48.10345>.
- [22] U. Schollwöck, Rev. Mod. Phys. **77**, 259 (2005), URL <https://link.aps.org/doi/10.1103/RevModPhys.77.259>.
- [23] Y.-F. Jiang, J. Zaanen, T. P. Devereaux, and H.-C. Jiang, Phys. Rev. Res. **2**, 033073 (2020), URL <https://link.aps.org/doi/10.1103/PhysRevResearch.2.033073>.
- [24] J. Jordan, R. Orús, G. Vidal, F. Verstraete, and J. I. Cirac, Phys. Rev. Lett. **101**, 250602 (2008), URL <https://link.aps.org/doi/10.1103/PhysRevLett.101.250602>.
- [25] N. V. Prokof'ev and B. V. Svistunov, Phys. Rev. Lett. **81**, 2514 (1998), URL <https://link.aps.org/doi/10.1103/PhysRevLett.81.2514>.
- [26] S. Zhang, J. Carlson, and J. E. Gubernatis, Phys. Rev. B **55**, 7464 (1997), URL <https://link.aps.org/doi/10.1103/PhysRevB.55.7464>.
- [27] A. Georges, G. Kotliar, W. Krauth, and M. J. Rozenberg, Rev. Mod. Phys. **68**, 13 (1996), URL <https://link.aps.org/doi/10.1103/RevModPhys.68.13>.
- [28] G. Knizia and G. K.-L. Chan, Phys. Rev. Lett. **109**, 186404 (2012), URL <https://link.aps.org/doi/10.1103/PhysRevLett.109.186404>.
- [29] T. Maier, M. Jarrell, T. Pruschke, and M. H. Hettler, Rev. Mod. Phys. **77**, 1027 (2005), URL <https://link.aps.org/doi/10.1103/RevModPhys.77.1027>.
- [30] W. Metzner, M. Salmhofer, C. Honerkamp, V. Meden, and K. Schönhammer, Rev. Mod. Phys. **84**, 299 (2012), URL <https://link.aps.org/doi/10.1103/RevModPhys.84.299>.
- [31] C.-C. Chang and S. Zhang, Phys. Rev. B **78**, 165101 (2008), URL <https://link.aps.org/doi/10.1103/PhysRevB.78.165101>.
- [32] M. Qin, H. Shi, and S. Zhang, Phys. Rev. B **94**, 235119 (2016), URL <https://link.aps.org/doi/10.1103/PhysRevB.94.235119>.
- [33] B.-X. Zheng, C.-M. Chung, P. Corboz, G. Ehlers, M.-P. Qin, R. M. Noack, H. Shi, S. R. White, S. Zhang, and G. K.-L. Chan, Science **358**, 1155 (2017), ISSN 0036-8075, <http://science.sciencemag.org/content/358/6367/1155.full.pdf>, URL <http://science.sciencemag.org/content/358/6367/1155>.
- [34] A. Damascelli, Z. Hussain, and Z.-X. Shen, Rev. Mod. Phys. **75**, 473 (2003), URL <https://link.aps.org/doi/10.1103/RevModPhys.75.473>.
- [35] O. Andersen, A. Liechtenstein, O. Jepsen, and F. Paulsen, Journal of Physics and Chemistry of Solids **56**, 1573 (1995), ISSN 0022-3697, proceedings of the Conference on Spectroscopies in Novel Superconductors, URL <http://www.sciencedirect.com/science/article/pii/0022369795002693>.
- [36] M. Hirayama, Y. Yamaji, T. Misawa, and M. Imada, Phys. Rev. B **98**, 134501 (2018), URL <https://link.aps.org/doi/10.1103/PhysRevB.98.134501>.
- [37] A better proxy for  $T_c$  might be the magnitude of the superconducting gap. This would be more difficult to calculate, and it also is only roughly tied to  $T_c$ .
- [38] V. J. Emery and S. A. Kivelson, Nature **374**, 434 (1995).



- [39] D. J. Scalapino, Rev. Mod. Phys. **84**, 1383 (2012), URL <https://link.aps.org/doi/10.1103/RevModPhys.84.1383>.
- [40] E. W. Huang, C. B. Mendl, H.-C. Jiang, B. Moritz, and T. P. Devereaux, npj Quantum Materials **3** (2018), URL <https://doi.org/10.1038%2Fs41535-018-0097-0>.
- [41] J. M. Tranquada, B. J. Sternlieb, J. D. Axe, Y. Nakamura, and S. Uchida, Nature **375**, 561 (1995).
- [42] J. M. Tranquada, Advances in Physics **69**, 437 (2020), <https://doi.org/10.1080/00018732.2021.1935698>, URL <https://doi.org/10.1080/00018732.2021.1935698>.
- [43] S. Jiang, D. J. Scalapino, and S. R. White, Proceedings of the National Academy of Sciences **118**, e2109978118 (2021), <https://www.pnas.org/doi/pdf/10.1073/pnas.2109978118>, URL <https://www.pnas.org/doi/abs/10.1073/pnas.2109978118>.
- [44] S. Gong, W. Zhu, and D. N. Sheng, Phys. Rev. Lett. **127**, 097003 (2021), URL <https://link.aps.org/doi/10.1103/PhysRevLett.127.097003>.
- [45] H.-C. Jiang and S. A. Kivelson, Phys. Rev. Lett. **127**, 097002 (2021), URL <https://link.aps.org/doi/10.1103/PhysRevLett.127.097002>.
- [46] H.-C. Jiang, S. A. Kivelson, and D.-H. Lee, *Superconducting valence bond fluid in lightly doped 8-leg t-j cylinders* (2023), URL <https://arxiv.org/abs/2302.11633>.
- [47] H.-C. Jiang and T. P. Devereaux, Science **365**, 1424 (2019), 1806.01465.
- [48] C.-M. Chung, M. Qin, S. Zhang, U. Schollwöck, and S. R. White (The Simons Collaboration on the Many-Electron Problem), Phys. Rev. B **102**, 041106 (2020), URL <https://link.aps.org/doi/10.1103/PhysRevB.102.041106>.
- [49] C.-C. Chang and S. Zhang, Phys. Rev. Lett. **104**, 116402 (2010), URL <https://link.aps.org/doi/10.1103/PhysRevLett.104.116402>.
- [50] H. Xu, H. Shi, E. Vitali, M. Qin, and S. Zhang, Phys. Rev. Research **4**, 013239 (2022), URL <https://link.aps.org/doi/10.1103/PhysRevResearch.4.013239>.
- [51] S. R. White and D. J. Scalapino, Phys. Rev. B **60**, R753 (1999), URL <https://link.aps.org/doi/10.1103/PhysRevB.60.R753>.
- [52] E. Fradkin, S. A. Kivelson, and J. M. Tranquada, Rev. Mod. Phys. **87**, 457 (2015), URL <https://link.aps.org/doi/10.1103/RevModPhys.87.457>.
- [53] M. Fishman, S. R. White, and E. M. Stoudenmire, SciPost Phys. Codebases p. 4 (2022), URL <https://scipost.org/10.21468/SciPostPhysCodeb.4>.
- [54] C. Hubig, F. Lachenmaier, N.-O. Linden, T. Reinhard, L. Stenzel, A. Swoboda, M. Grundner, and S. M. add other contributors here, *The SYTEN toolkit*, URL <https://syten.eu>.
- [55] C. Lin, F. H. Zong, and D. M. Ceperley, Phys. Rev. E **64**, 016702 (2001), URL <https://link.aps.org/doi/10.1103/PhysRevE.64.016702>.
- [56] M. Qin, H. Shi, and S. Zhang, Phys. Rev. B **94**, 085103 (2016), URL <https://link.aps.org/doi/10.1103/PhysRevB.94.085103>.
- [57] Y. Gannot and S. A. Kivelson, Phys. Rev. B **107**, 075127 (2023), URL <https://link.aps.org/doi/10.1103/PhysRevB.107.075127>.
- [58] Z. Chen, Y. Wang, S. N. Rebec, T. Jia, M. Hashimoto, D. Lu, B. Moritz, R. G. Moore, T. P. Devereaux, and Z.-X. Shen, Science **373**, 1235 (2021), <https://www.science.org/doi/pdf/10.1126/science.abf5174>, URL <https://www.science.org/doi/abs/10.1126/science.abf5174>.
- [59] S. Jiang, D. J. Scalapino, and S. R. White, arXiv e-prints arXiv:2303.00756 (2023), 2303.00756.

# Supplementary materials for “coexistence of superconductivity with partially filled stripes in the Hubbard model”

Hao Xu,<sup>1,\*</sup> Chia-Min Chung,<sup>2,3,4,\*</sup> Mingpu Qin,<sup>5</sup> Ulrich Schollwöck,<sup>6,7</sup> Steven R. White,<sup>8</sup> and Shiwei Zhang<sup>9</sup>

<sup>1</sup>*Department of Physics, College of William and Mary, Williamsburg, Virginia 23187, USA*

<sup>2</sup>*Department of Physics, National Sun Yat-sen University, Kaohsiung 80424, Taiwan*

<sup>3</sup>*Center for Theoretical and Computational Physics,*

*National Sun Yat-Sen University, Kaohsiung 80424, Taiwan*

<sup>4</sup>*Physics Division, National Center for Theoretical Sciences, Taipei 10617, Taiwan*

<sup>5</sup>*Key Laboratory of Artificial Structures and Quantum Control,*

*School of Physics and Astronomy, Shanghai Jiao Tong University, Shanghai 200240, China*

<sup>6</sup>*Arnold Sommerfeld Center for Theoretical Physics,*

*Ludwig-Maximilians-Universität München, 80333 Munich, Germany*

<sup>7</sup>*Munich Center for Quantum Science and Technology (MCQST), 80799 Munich, Germany*

<sup>8</sup>*Department of Physics and Astronomy, University of California, Irvine, California 92697, USA*

<sup>9</sup>*Center for Computational Quantum Physics, Flatiron Institute, New York, NY 10010, USA*

## I. PARTIAL PARTICLE-HOLE TRANSFORMATION OF THE HUBBARD MODEL

When pairing fields are applied in the Hubbard model, the total particle number is not conserved. The usual ground-state AFQMC is formulated in the space of Slater determinant with a fixed electron number. While a more general solution is to reformulate AFQMC in Hartree-Fock-Bogoliubov (HFB) space [1], the problem here can be solved without modifying the AFQMC codes, by applying a partial particle-hole transformation [2]

$$\begin{aligned} \hat{c}_{i\uparrow} &\rightarrow \hat{d}_{i\uparrow}, & \hat{c}_{i\uparrow}^\dagger &\rightarrow \hat{d}_{i\uparrow}^\dagger \\ \hat{c}_{i\downarrow} &\rightarrow \hat{d}_{i\downarrow}(-1)^i, & \hat{c}_{i\downarrow}^\dagger &\rightarrow \hat{d}_{i\downarrow}^\dagger(-1)^i, \end{aligned} \quad (1)$$

where  $i$  labels the lattice sites in the bipartite lattice. With this transformation, the  $t'$  Hubbard Hamiltonian in Eq. (1) in the main text turns into

$$\begin{aligned} \hat{H} &= -t \sum_{\langle i,j \rangle \sigma} \hat{d}_{i\sigma}^\dagger \hat{d}_{j\sigma} - t' \sum_{\langle\langle i,j \rangle\rangle \sigma} s(\sigma) \hat{d}_{i\sigma}^\dagger \hat{d}_{j\sigma} \\ &+ U \sum_i (\hat{m}_{i\uparrow} - \hat{m}_{i\downarrow} \hat{m}_{i\uparrow}) - \mu \sum_i (\hat{m}_{i\uparrow} + 1 - \hat{m}_{i\downarrow}), \end{aligned} \quad (2)$$

where  $s(\uparrow) = +1$  and  $s(\downarrow) = -1$ , and  $\hat{m}_{i,\sigma} = \hat{d}_{i,\sigma}^\dagger \hat{d}_{i,\sigma}$ . Note that the next near-neighbor hopping changes sign for down spins after the transformation. The pairing operator  $\hat{\Delta}_{ij} = (\hat{c}_{i\uparrow} \hat{c}_{j\downarrow} - \hat{c}_{i\downarrow} \hat{c}_{j\uparrow})/\sqrt{2}$  is transformed to:

$$\hat{\Delta}_{ij} = ((-1)^{j+1} \hat{d}_{j\downarrow}^\dagger \hat{d}_{i\uparrow} - (-1)^i \hat{d}_{i\downarrow}^\dagger \hat{d}_{j\uparrow})/\sqrt{2} \quad (3)$$

which is now a spin-flip hopping term. The sign of  $U$  is reversed, meaning the interaction turns to attractive. Up and down electron now acquire effective chemical potentials  $\mu - U$  and  $-\mu$ , respectively, which means

$(\sum_i \langle \hat{m}_{i\uparrow} \rangle \neq \sum_i \langle \hat{m}_{i\downarrow} \rangle)$ . After the transformation we have

$$\sum_i (\hat{m}_{i\uparrow} + \hat{m}_{i\downarrow}) = \sum_i (\hat{n}_{i\uparrow} + 1 - \hat{n}_{i\downarrow}) = N_s, \quad (4)$$

such that the total number of electrons equals the number of sites, i.e., the system is at half-filling but with spin imbalance. The random walkers (Slater determinants) are now represented as  $2N \times N_e$  matrix [3] in the AFQMC calculation, and each orbital in the Slater determinant is now a spin-orbital with a mixture of up and down components.

## II. TWIST BOUNDARY CONDITIONS

Twist boundary conditions (TBC) in  $x$ -direction means the wave-function satisfies:

$$\psi(\mathbf{r}_1 + L\hat{e}_x, \mathbf{r}_2, \dots, \mathbf{r}_N) = e^{i\theta_x} \psi(\mathbf{r}_1, \mathbf{r}_2, \dots, \mathbf{r}_N). \quad (5)$$

For convenience we have used  $L$  to denote  $L_x$ , the linear dimension of the periodic cell in  $x$ -direction. (The definitions of TBC in other directions are similar). For the two dimensional systems studied in this work, the phases for the two directions are independent of each other, and the phase factors from  $x$ - and  $y$ -directions are multiplicative. Thus, with no loss of generality, we will only explicitly write out one dimension ( $x$ ) below. We will assume that the lattice sites are labeled from 1 to  $L$ .

Different gauges can be adopted to realize TBC. We discuss two common choices here. In gauge A, an electron picks up a phase only when it crosses the boundary, while in gauge B, the phase is split over all bonds evenly.

### A. Gauge A

In gauge A, if we apply the same twist for  $\uparrow$  and  $\downarrow$ -spins in the repulsive Hubbard model, we have

$$\begin{aligned} c_{L+1,\sigma}^\dagger &= \exp(i\theta) c_{1,\sigma}^\dagger \\ c_{L+1,\sigma} &= \exp(-i\theta) c_{1,\sigma} \end{aligned} \quad (6)$$

\*These two authors contributed equally to this work.

So the hopping between the last and first site is modified as

$$-t\hat{c}_{1\sigma}^\dagger\hat{c}_{L\sigma} + h.c \rightarrow -t\exp(i\theta)\hat{c}_{1\sigma}^\dagger\hat{c}_{L\sigma} + h.c \quad (7)$$

while the other hopping terms remains unchanged. After the partial particle-hole transformation in Eq. (1), the spin up term is unchanged, but the phase for down spin changes to  $-\theta$  as

$$-t\exp(-i\theta)\hat{d}_{1\downarrow}^\dagger\hat{d}_{L\downarrow} + h.c \quad (8)$$

The same is true for the  $t'$  term.

With TBC, we also need to modify the definition of the pairing operator ( $\hat{\Delta}_{kj} = (\hat{c}_{k\uparrow}\hat{c}_{j\downarrow} - \hat{c}_{k\downarrow}\hat{c}_{j\uparrow})/\sqrt{2}$ , for bonds connecting nearest-neighbor sites,  $\langle jk \rangle$ ) for the bond connecting the first and last site as

$$\hat{\Delta}_{1L} = \exp(-i\theta)(\hat{c}_{1\uparrow}\hat{c}_{L\downarrow} - \hat{c}_{1\downarrow}\hat{c}_{L\uparrow})/\sqrt{2}. \quad (9)$$

When applying the pairing field to calculate the pairing order, we need to include the phase in Eq. (9) when twist boundary conditions are imposed. In the AFQMC calculation, the pairing operator in Eq. (9) can be transformed, following Eq. (1), as

$$\hat{\Delta}_{1L} = \exp(-i\theta)(\hat{d}_{1\downarrow}^\dagger\hat{d}_{L\uparrow} - (-1)^L\hat{d}_{L\downarrow}^\dagger\hat{d}_{1\uparrow})/\sqrt{2} \quad (10)$$

Other pairing terms are transformed to the  $-U$  case following Eq. (3)

## B. Gauge B

We next consider gauge B in a similar setup to Gauge A. Now the phase is spread evenly over each bond and we have, for the repulsive model

$$\begin{aligned} c_{j\sigma}^\dagger &\rightarrow c_{j\sigma}^\dagger \exp(i(j-1)\frac{\theta}{L}) \\ c_{j\sigma} &\rightarrow c_{j\sigma} \exp(-i(j-1)\frac{\theta}{L}) \end{aligned} \quad (11)$$

and

$$\begin{aligned} c_{L+1,\sigma}^\dagger &= \exp(i\theta)c_{1,\sigma}^\dagger \\ c_{L+1,\sigma} &= \exp(-i\theta)c_{1,\sigma} \end{aligned} \quad (12)$$

The nearest neighbor hopping term is then modified to

$$-t \sum_j \exp(i\theta/L)\hat{c}_{j+1\sigma}^\dagger\hat{c}_{j\sigma} + h.c. \quad (13)$$

The  $t'$  term has similar form.

The pairing operator  $\hat{\Delta}_{kj} = (\hat{c}_{k\uparrow}\hat{c}_{j\downarrow} - \hat{c}_{k\downarrow}\hat{c}_{j\uparrow})/\sqrt{2}$  is modified as

$$\hat{\Delta}_{kj} = (\hat{c}_{k\uparrow}\hat{c}_{j\downarrow} - \hat{c}_{k\downarrow}\hat{c}_{j\uparrow}) \exp(-i(k+j-2)\theta/L)/\sqrt{2} \quad (14)$$

For the bond connecting the first and last site, we have

$$\hat{\Delta}_{L,1} = (\hat{c}_{L\uparrow}\hat{c}_{1\downarrow} - \hat{c}_{1\downarrow}\hat{c}_{L\uparrow}) \exp(-i(2L-1)\theta/L)/\sqrt{2} \quad (15)$$

We can then follow the particle-hole transformation in Eq. (1) to transform the definition of pairing order to the negative  $U$  model, which is used in the AFQMC calculation.

## C. The equivalence of the two gauges

The two gauges discussed above are equivalent and physical quantities should have the same values under them, which we have explicitly verified. Since the interaction term is independent of the twist angle, it is convenient to test the TBC implementation in non-interacting systems. For example, in a  $20 \times 4$  lattice with  $t' = -0.2t$ ,  $\mu = 0.8$ , and twist angle  $\theta_x = 1.2994\pi$ ,  $\theta_y = 0.6026\pi$ , it is easily checked in all our codes that physical quantities, such as the energy per site ( $-1.15861112$ ), average pairing order per bond ( $0.01108939$ ), and the electron density ( $0.82422077$ ), are all exactly the same under the two gauges.

## III. SELF-CONSISTENT CONSTRAINT IN AFQMC

We apply magnetic and pairing pinning fields to probe the corresponding response in the studied systems. A self-consistent procedure in AFQMC allows us to apply a constraint to remove the sign problem. We describe the pinning field calculations and the self-consistency procedure below.

The magnetic pinning fields are typically applied in cylindrical cells, to one or both ends of the cylinder, not in the rest of the cell. We try different configurations of the magnetic pinning fields to probe the possible magnetic order or correlation. The strength of the fields is fixed at  $h_m = 0.25$ , and limited to only the edge(s) of the cylinder. For most of the systems, we applied anti-ferromagnetic pinning fields at the open edges of the studied cylinders ( $(-1)^{(i_x+i_y)}h_m$  for  $i_x = 1$  and  $L_x$ ). In some cases, we also test a pinning field configuration with a  $\pi$  phase to the pinning magnetic fields on the right edge as  $((-1)^{(i_x+i_y)}h_m$  for  $i_x = 1$  and  $(-1)^{(i_x+i_y+1)}h_m$  for  $i_x = L_x$ ), and compare the energies to determine the true ground state, the one with the lower energy. Note that it is important in this scheme to examine progressively larger (longer) systems, in order to remove the effect of the local pinning field. Ref. [4] includes further details of our analysis method and how we extract information in the TDL.

To compute the pairing order parameter, we apply global pairing fields across the entire simulation cell, similar to Ref. [2]. To probe the  $d$ -wave pairing response the applied pair-inducing fields on vertical and horizontal bonds have the same strength  $h_d$  but opposite signs. The Hamiltonian with pairing fields is

$$\hat{H}'(h_d) = \hat{H} + \hat{H}_d(h_d) \quad (16)$$

where

$$\hat{H}_d(h_d) = -h_d \sum_{\langle i,j \rangle} b_{ij} \frac{\hat{\Delta}_{ij} + \hat{\Delta}_{ij}^\dagger}{2}, \quad (17)$$

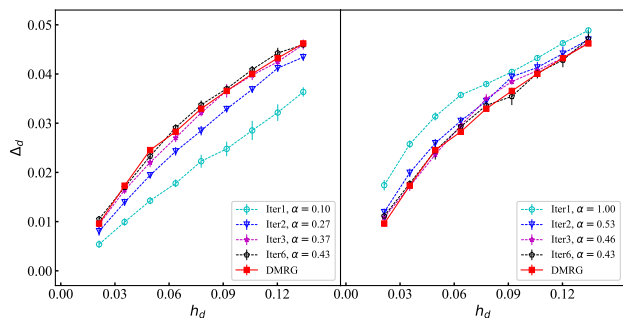


FIG. 1: Robustness of the self-consistent constraint in AFQMC. An example is shown for the pairing order parameter in the 1/4 hole-doped Hubbard model on a  $16 \times 4$  cylinder. On the left panel, the self-consistent calculation starts with an initial value of  $\alpha = 0.1$ . The calculation converges with a handful of iterations to the exact result (DMRG, red) in this system, with a converged value  $\alpha = 0.43$ . On the right panel, the calculation is initialized with  $\alpha = 1.0$ , and converges from the opposite direction to the same result.

where  $b_{ij} = +1$  for a bond connecting two nearest-neighbors  $i$  and  $j$  in the  $x$ -direction and  $b_{ij} = -1$  if  $\langle ij \rangle$  is in the  $y$ -direction.

The pairing order is calculated from the derivative of the ground state energy  $E'(h_d)$  with respect to  $h_d$ , following the Hellmann-Feynman theorem. Recall these calculations are performed in the particle-hole-transformed attractive Hubbard Hamiltonian in Eq. (2). We take the ground state of the non-interacting Hamiltonian ( $U = 0$  in Eq. (2)) with the pairing field  $\alpha h_d$  as trial wave function, where  $\alpha$  is a parameter to be determined in the self-consistent iterations. In the first step, we choose an arbitrary  $\alpha$  and calculate the average value of pairing order with AFQMC using the corresponding trial wave function as a constraint. We then tune the value of  $\alpha$  by minimizing the difference between the pairing orders given by the non-interacting wave-function and the previous iteration of AFQMC. We then carry out the next iteration AFQMC calculation with the new trial wave-function. This process is repeated until  $\alpha$  is converged. In each mean-field solution we tune the value of chemical potential to target the desired spin imbalance (i.e., the electron density in the repulsive model). In performing TABC, we determine the final value of  $\alpha$  via averaging over different twist angles. The value is found to converge quickly, so a small set of pilot calculations can be performed first to obtain a good estimate. More computations can be added if further precision is needed.

In Fig. 1, we show the computed pairing order in the self-consistent process for the 1/4 hole doped  $t'$  Hubbard model on a  $16 \times 4$  cylinder. DMRG results are also shown, because for this narrow system, it provides a reference result which is essentially exact. In Fig. 1, we start the self-consistent calculation with an initial value  $\alpha = 0.1$  (the left panel). After 6 iterations, the pairing order converges to the DMRG results. The converged value of  $\alpha$

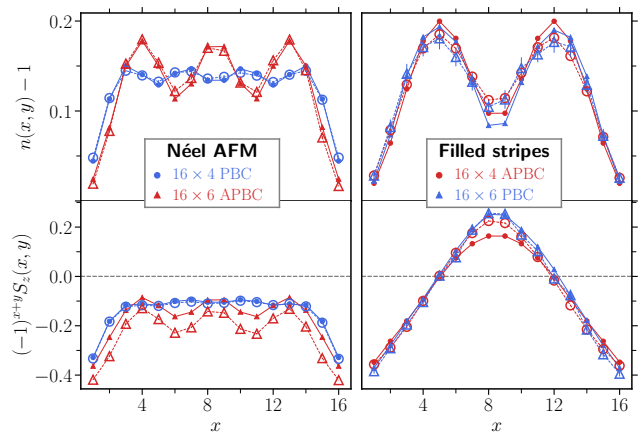


FIG. 2: Strong sensitivity of the spin and charge orders to system sizes and boundary conditions. Here we show results for four different systems, all with the same bulk parameters ( $\delta = 1/8$ , electron doped), but different in size and boundary conditions. Line cuts of the doped electron density (top panels) and staggered spin density (bottom) are shown, with combinations of two system sizes,  $16 \times 4$  and  $16 \times 6$ , and periodic (PBC) and antiperiodic (APBC) boundary conditions. Antiferromagnetic pinning fields have been applied at the left and right edges of the open cylinders. Two distinct types of states appear, Néel AFM with fairly uniform electron densities (left panels), and filled stripe states (right panels). Good agreement is found between DMRG (filled symbols) and AFQMC (empty symbols); the differences are tied to the sizes and boundary conditions.

is  $\alpha = 0.43$ . We also obtain the same converged pairing order and  $\alpha$  value by starting the self-consistent process with  $\alpha = 1.0$  (the right panel), indicating the self-consistent calculation is independent of the initial value of  $\alpha$ .

#### IV. SENSITIVITY OF ORDER TO SYSTEM SIZES AND BOUNDARY CONDITIONS

In Fig. 2 we show an example of the strong sensitivity of the ground states to system sizes and boundary conditions (BCs). Two entirely different ground states are obtained for the same physical parameters from four different combinations of size/BCs, with an alternation between the effects of size versus BC. Consistent results are seen from both methods. This sort of sensitivity is also observed on the hole-doped side (see Fig. 4). To determine the order in the thermodynamic limit in these systems thus requires computations in significantly larger sizes than has been previously reached. Below, we also show the presence of numerous low-lying states whose ordering in energy can be affected by size and BCs. In many cases these low-lying states can be tied to different stripe configurations. In the case of Fig. 2, the system may be close to a phase boundary between the two types of states[5]. The twist-averaging procedure

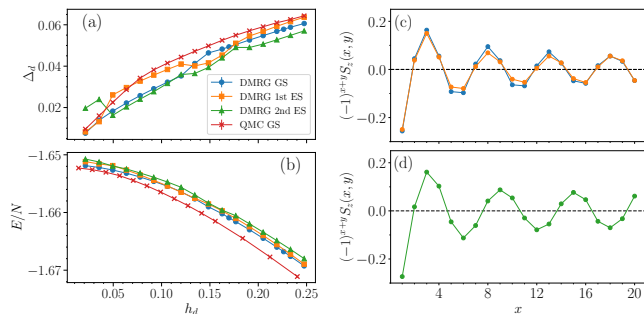


FIG. 3: Illustration of low-lying states and level-crossing. The pairing order  $\Delta_d$  (a) and energy per site (b) are shown as functions of the global pairing field strength  $h_d$  for a  $1/5$  hole doped system in a  $20 \times 4$  cylinder. The error bars are smaller than the symbol sizes. In (c) and (d) the staggered spin densities are shown along the  $x$  direction for the three low-lying states from DMRG, for  $h_d \approx 0.0075$ , the smallest  $h_d$  we consider. The AF magnetic pinning fields are applied at the left open edge.

adopted here tends to average over the various states, which allows better extrapolation to the TDL compared to earlier approaches[6].

## V. LEVEL CROSSING WITH APPLIED PAIRING FIELDS

In addition to the enhanced sensitivity of the ground state to the boundary conditions and system sizes in the  $t'$  Hubbard model, the evolution of the ground state with the strength of the applied pairing field is subtle, and creates another computational challenge. In Fig. 3 (a) and (b), as an example, we show the evolution of a few low-lying states as a function of  $h_d$ , in a  $20 \times 4$  system at  $1/5$  hole doping. As  $h_d$  decreases, the low-lying states, which are separated by tiny energy differences (note the small energy scale in b), exhibit crossovers between several branches. The different branches are characterized by different numbers of stripes in the states, as shown in Fig. 3 (c) and (d). That  $d$ -wave pairing field induces strong level crossings is another indication of the intimate connection between the fluctuation of the stripe state and superconductivity in the system. As mentioned, such level-crossings make the comparisons between DMRG and AFQMC more challenging, as each calculation is often sensitive to even small variations in the calculational parameters. However this effect is reduced by employing twist averaging, in which all the low-lying states are sampled. As can be seen in Fig. 5 in the main text, TABC effectively treats the crossovers as a function of  $h_d$ , which results in smooth curves, and DMRG and AFQMC agree very well.

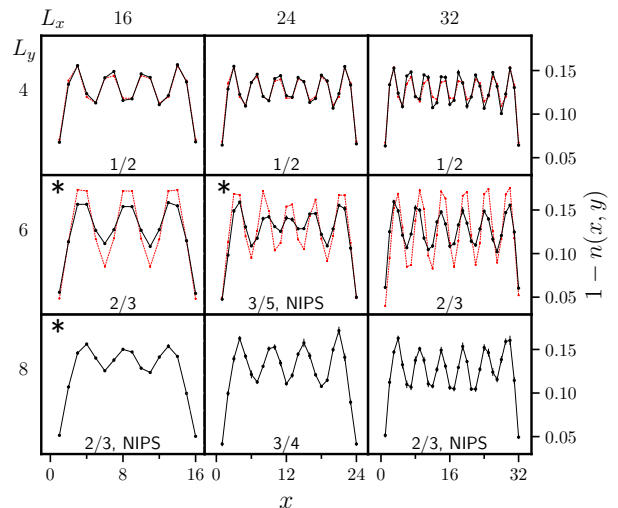


FIG. 4: Hole density for the systems in Fig. 2 in the main text for  $1/8$  hole doping. The evolution of the stripe patterns is shown versus system size. The hole densities are shown as linecuts along the length of the cylinders. The length of the cylinder ( $L_x$ ) is varied across the three columns and the width ( $L_y$ ) across rows. AFM pinning fields are applied at the two edges of the cylinder ( $x = 1$  and  $x = L_x$ ), either in phase or with a  $\pi$ -phase shift (marked by an asterisk); the one with lower energy is shown. The filling fraction  $f$  of each stripe pattern is indicated, with NIPS denoting non integer-pair stripes. DMRG results (red) are shown for width-4 and 6 systems, and AFQMC (black) are in good agreement with them.

## VI. SUPPLEMENTAL DATA

### A. Hole density for $1/8$ hole doped systems

In Fig. 4, we show the hole density for the systems in Fig. 2 in the main text. For systems with width 4 and 6, for which DMRG is available, we find good agreement between AFQMC and DMRG results. In width-6 systems, the discrepancies are somewhat larger in the density here compared to the spin in Fig. 2 in the main text. This is likely because of a combination of two factors. First AFQMC has shown in  $t' = 0$  Hubbard model a slight tendency to under-estimate the amplitude of the density fluctuations in stripes [4, 7]. Second, in some cases we have seen indications that the DMRG may not have reached full convergence in width-6 systems, even with the very large bond dimensions we were able to do.

### B. Additional data on pairing order parameter

In this subsection, we include the finite size data for the pairing order, as well as the extrapolation process to obtain the spontaneous pairing order in the thermodynamic limit which is plotted in Fig. 1 in the main text.



### 1. Electron doped region

In Figs. 5, 6, and 7 we present the data for pairing order in the electron-doped region, with  $\delta = 1/8, 1/5,$  and  $1/3$  respectively. As discussed in the main text, we use fully periodic systems (i.e., torus simulation cells of  $L_x \times L_y$ ) and perform TABC with quasi-random twists. We have verified that the results have converged with respect to  $L_x$  to within our statistical error. When extrapolating the pairing orders with width of the system, we omit width-4 systems. When extrapolating the TDL values versus  $h_d$ , we perform both linear and quadratic fits. In the linear fits, we use  $h_d < 0.05$ , when the data is clearly in the linear response regime. In the quadratic fits, we include more data points, 10-12 values of  $h_d$ . We find that the resulting extrapolated  $\Delta_d(h_d \rightarrow 0)$  values are

often indistinguishable. When there is a difference, the result from the better fit (smaller  $\chi^2$ ) is used. The final pairing order at TDL is 0.007(3), 0.007(4), and 0.000(2) for  $\delta = 1/8, 1/5,$  and  $1/3$ , respectively, as reported in Fig. 1 in the main text.

### 2. Hole doped region

In Figs. 8, 9, 10, and 11 we present the data for pairing order in the hole-doped region, with  $\delta = 1/8, 1/5, 1/4,$  and  $1/3$  respectively. The final pairing order at TDL for  $\delta = 1/8, 1/5, 1/4,$  and  $1/3$  are 0.017(3), 0.016(2), 0.007(3), and 0.002(3), as shown in Fig. 1 in the main text.

- 
- [1] H. Shi and S. Zhang, Phys. Rev. B **95**, 045144 (2017), URL <https://link.aps.org/doi/10.1103/PhysRevB.95.045144>.
- [2] M. Qin, C.-M. Chung, H. Shi, E. Vitali, C. Hubig, U. Schollwöck, S. R. White, and S. Zhang (Simons Collaboration on the Many-Electron Problem), Phys. Rev. X **10**, 031016 (2020), URL <https://link.aps.org/doi/10.1103/PhysRevX.10.031016>.
- [3] M. Qin, H. Shi, and S. Zhang, Phys. Rev. B **94**, 085103 (2016), URL <https://link.aps.org/doi/10.1103/PhysRevB.94.085103>.
- [4] H. Xu, H. Shi, E. Vitali, M. Qin, and S. Zhang, Phys. Rev. Research **4**, 013239 (2022), URL <https://link.aps.org/doi/10.1103/PhysRevResearch.4.013239>.
- [5] S. Jiang, D. J. Scalapino, and S. R. White, Proceedings of the National Academy of Sciences **118**, e2109978118 (2021), <https://www.pnas.org/doi/pdf/10.1073/pnas.2109978118>, URL <https://www.pnas.org/doi/abs/10.1073/pnas.2109978118>.
- [6] H.-C. Jiang and T. P. Devereaux, Science **365**, 1424 (2019), 1806.01465.
- [7] M. Qin, H. Shi, and S. Zhang, Phys. Rev. B **94**, 235119 (2016), URL <https://link.aps.org/doi/10.1103/PhysRevB.94.235119>.

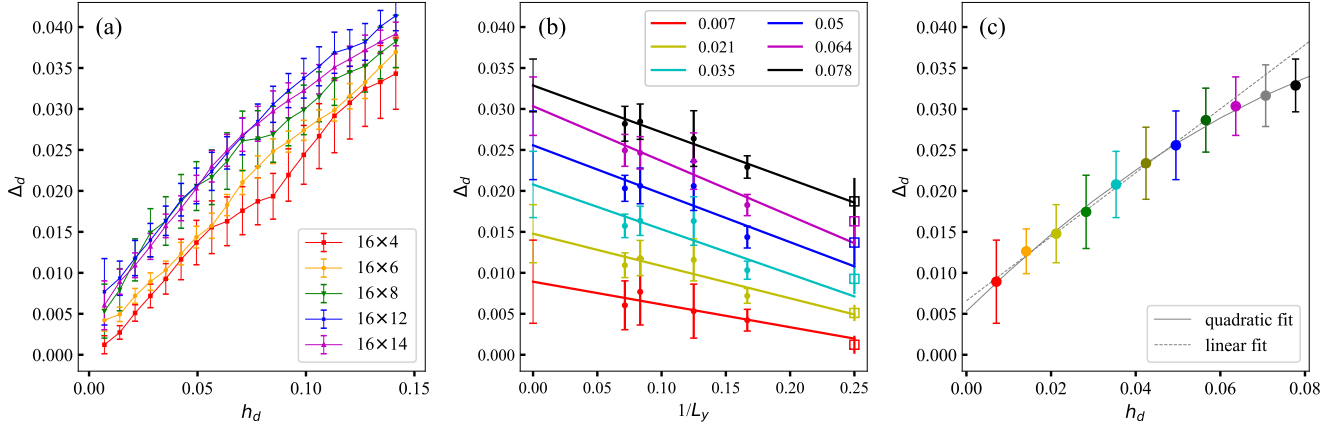


FIG. 5: The extrapolation of pairing order for 1/8 electron doping. (a) shows the pairing order parameter versus pairing field for different system sizes. The data for each torus of  $L_x \times L_y$  is obtained from TABC with quasi-random twists  $(k_x, k_y)$ . The number of twists is a few dozens for smaller systems and about a dozen for the larger systems. (b) shows extrapolation of the pairing order with the width of the system for each fixed pairing field. In (c) the extrapolated value in (b) is plotted against pairing field and then an extrapolation of the pairing field to  $h_d \rightarrow 0$  gives the spontaneous pairing order at thermodynamic limit. Both linear and quadratic fits give consistent results.

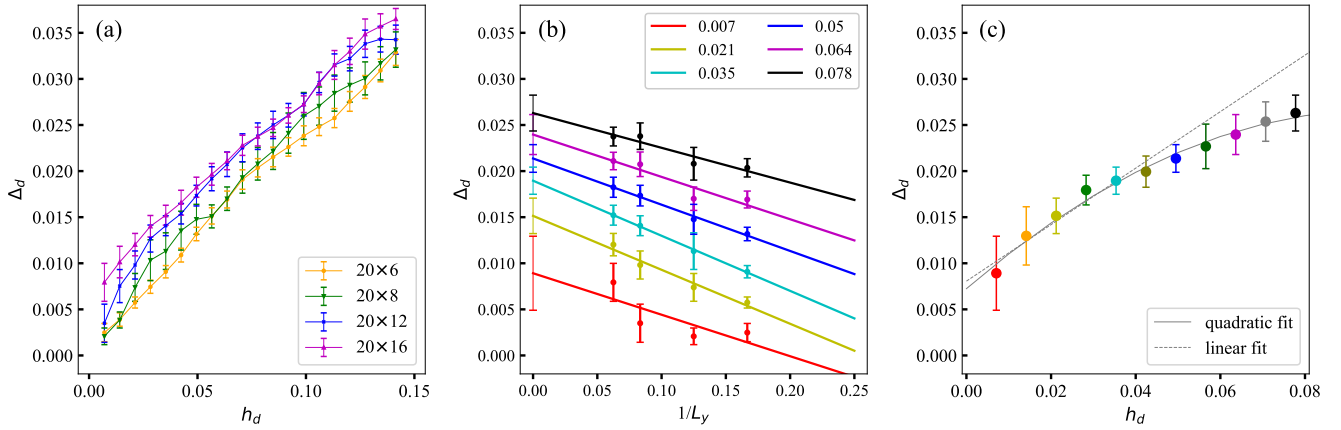


FIG. 6: Similar as Fig. 5 but for 1/5 electron doping.

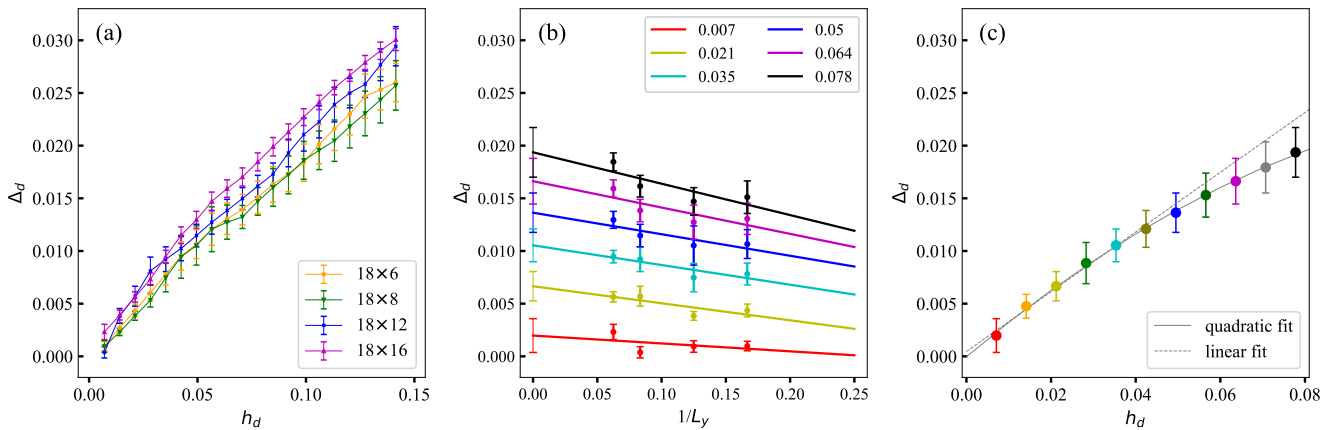


FIG. 7: Similar as Fig. 5 but for 1/3 electron doping.

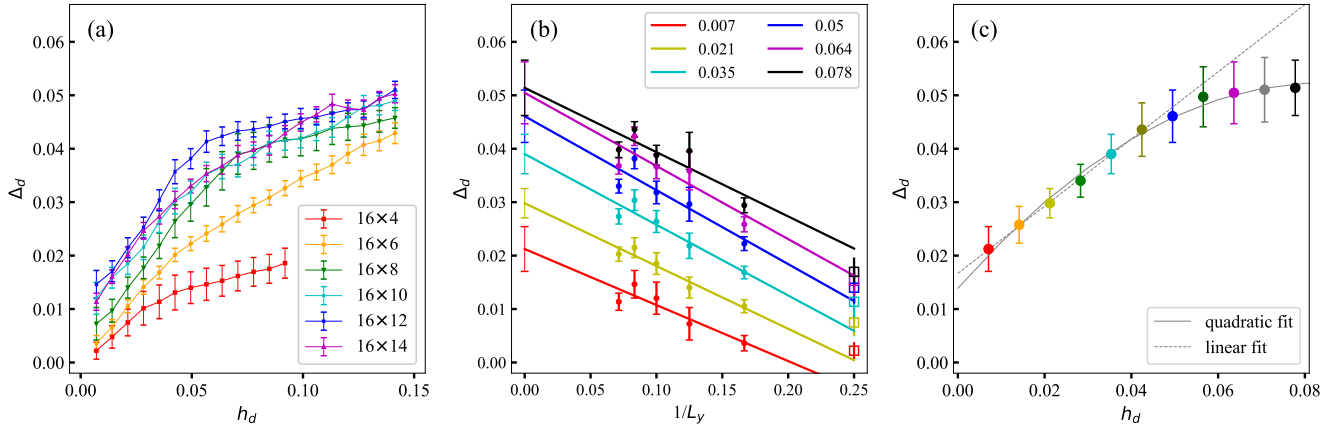


FIG. 8: Similar as Fig. 5 but for 1/8 hole doping.

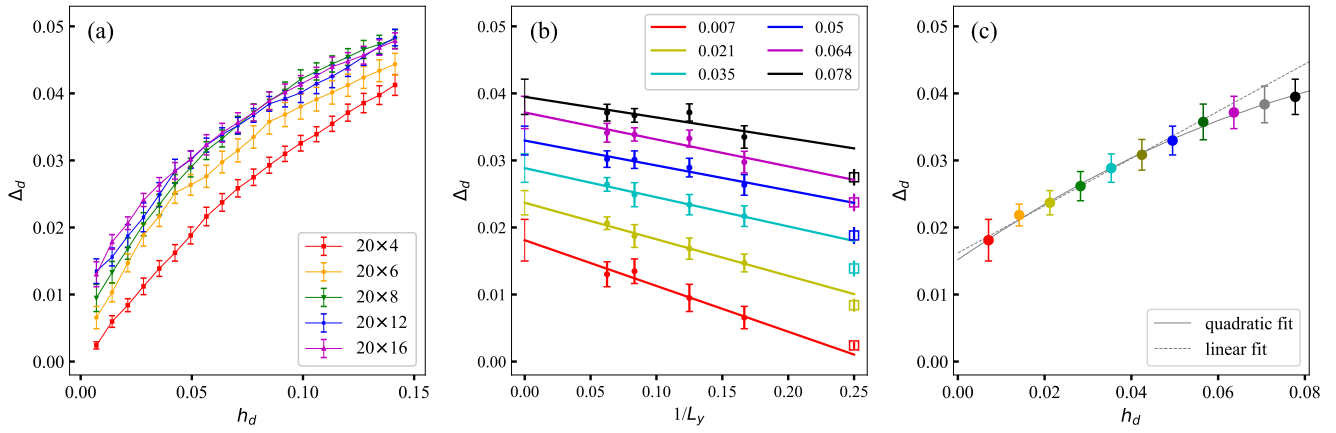


FIG. 9: Similar as Fig. 5 but for 1/5 hole doping.

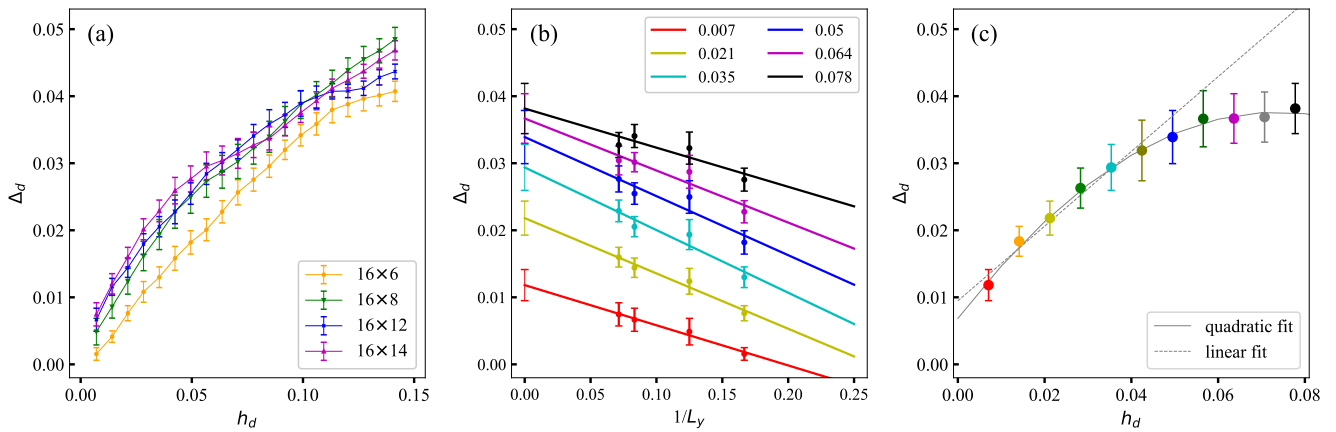


FIG. 10: Similar as Fig. 5 but for 1/4 hole doping.

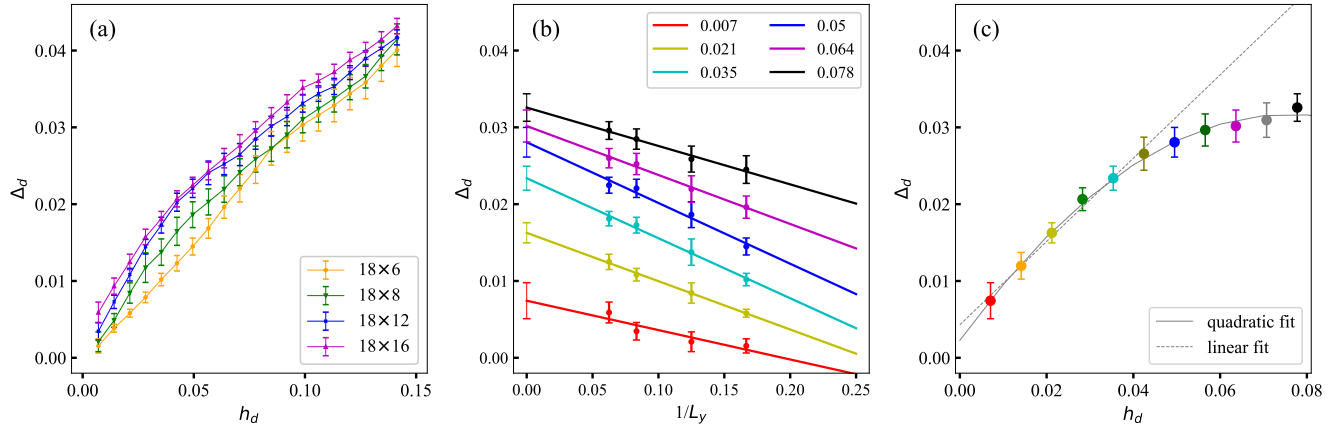


FIG. 11: Similar as Fig. 5 but for 1/3 hole doping.